

# Implementation of a Skull-Conformal Phased Array for Transcranial Focused Ultrasound Therapy

Chris Adams, *Member, IEEE*, Ryan M. Jones, *Member, IEEE*, Steven D. Yang, Wai Meng Kan, Kogee Leung, Yuheng Zhou, Kang Uk Lee, Yuexi Huang, and Kullervo Hynynen, *Fellow, IEEE*

**Abstract—Objective:** To implement a skull-conformal phased array for ultrasound-guided transcranial focused ultrasound therapy with improved patient comfort. **Methods:** Using patient-specific computed tomography and MRI neuroimaging data, tightly-conforming helmet scaffolds were designed computationally. The helmet scaffolds were designed to hold reusable transducer modules at near-normal incidence in an optimal configuration for the treatment location(s) of interest. Numerical simulations of trans-skull ultrasound propagation were performed to evaluate different conformal array designs and to compare with hemispherical arrays similar to those employed clinically. A 4096-element phased array was constructed by 3D printing a helmet scaffold optimised for an ex vivo human skullcap, and its performance was evaluated via benchtop and in vivo experiments. **Results:** Acoustic field measurements confirmed the system's ability to focus through human skull bone using simulation-based transcranial aberration corrections. Preliminary in vivo testing demonstrated safe trans-human skull blood-brain barrier (BBB) opening in rodents. **Conclusion:** Patient-specific conformal ultrasound phased arrays appear to be a feasible and safe approach for conducting transcranial BBB opening procedures. **Significance:** Skull-conformal phased arrays stand to improve patient comfort and have the potential to accelerate the adoption of transcranial FUS therapy by improving access to the technology.

**Index Terms—**focused ultrasound, image guided therapy, conformal phased arrays, personalised medicine.

## I. INTRODUCTION

ADVANCES in transcranial focused ultrasound (FUS) have made treatment possible for many conditions that would otherwise be highly invasive or risk adverse to remediate. When thermal treatment mechanisms are sought, continuous-wave, high powered FUS can be leveraged to

All authors are with the Physical Sciences Platform, Sunnybrook Research Institute, Toronto, ON, Canada. Authors Chris Adams and Kullervo Hynynen are also with the Department of Medical Biophysics, University of Toronto, Toronto, ON, Canada. This work was supported by the W. Garfield Weston Foundation, the National Institute of Biomedical Imaging and Bioengineering of the National Institutes of Health (grant number: R01 EB003268), the Canadian Institutes of Health Research (grant number: FDN 154272), the Temerty Chair in Focused Ultrasound Research at Sunnybrook Health Sciences Centre, and support from Beamish and Connor foundations. Contact: christopher.adams@sri.utoronto.ca, khynynen@sri.utoronto.ca

selectively heat [1] or necrose tissue via thermal coagulation, while sparing surrounding brain regions [2], [3]. Transcranial FUS thermoablation is being investigated for a variety of conditions including brain tumours [4] as well as movement [5]–[7] and psychiatric disorders [8]. Alternatively, pulsed FUS in combination with pre-formed microbubbles typically used in diagnostic ultrasound [9] can be exploited to induce bio-effects [10] and modulate the permeability of the blood-brain barrier (BBB) [11] for targeted drug delivery to the brain. This technique is also being explored to treat brain tumours [12], [13] as well as several neurological disorders, including Alzheimer's disease [14], [15] and Amyotrophic Lateral Sclerosis [16].

Historically, the presence of the skull introduced many technical challenges in providing FUS therapy to the brain [17]. Due to the high acoustic impedance mismatch between bone and soft tissues, the human skull prevents effective transmission of ultrasound energy by reflection [18]. In addition, ultrasound propagation within the bone itself is highly attenuating, particularly at high frequencies [19]. Another major challenge is that due to the varying thickness and density of cranial bone, and large differences in longitudinal sound speed between bone and tissue, the skull in effect acts as a de-focusing lens [20].

Hemispherical phased-arrays [21] with magnetic resonance imaging (MRI) guidance are most commonly used in a clinical setting. Here, elements of the array are densely distributed on a hemisphere and are excited with different phases and amplitudes to compensate for the aberrations induced by the skull. Phase and amplitude values are obtained using computed tomography (CT) data combined with measurements of skull density, shape, thickness and experimental speed of sound measurements [22], [23]. The MRI is used to guide therapy and provide thermometry information during thermal treatments [24].

In the context of BBB opening, no device been approved for clinical use yet. Outside of FUS mediated BBB opening, some techniques for the circumvention of the BBB for drug delivery include hyperosmotic solutions [25], carrier protein mediated transport [26] and intracranial injections [27] amongst others. Compared with these techniques, FUS mediated BBB-opening has the advantage of being non-invasive and targeted [28]. Increases in vascular permeability following FUS thermal

treatments were first observed at the periphery of lesions [29]. Thermally-induced increase in the permeability of the BBB has been demonstrated, but was often accompanied by tissue damage and inconsistent results. However, introducing clinically-approved diagnostic microbubbles makes FUS-mediated BBB opening reliable while minimising neuronal damage [30]. With optimised FUS parameters it possible to open the BBB without evidence of permanent damage and with acute inflammatory response [31].

Hemispherical designs are well suited to thermal treatments as they maximise skull transmission area, and thus minimise average skull heating [21]. However, for bubble-mediated treatments, another design may be optimal. Some of the first clinical trials of BBB opening were using implantable devices [32]–[34]. Single element-devices assisted by neuronavigation [35], [36] have shown to be feasibly comparable in precision to stereotactic procedures without requiring MR guidance. Authors continue to explore alternative techniques for circumventing the de-focusing effect of the skull [37] and for acquiring phase corrections ultrasonically [38]–[43] and with MR [44], [45].

The Insightec (INSIGHTEC Ltd., Tirat Carmel, Israel) clinically-approved arrays use a hemispherical array of sufficient radius (15 cm) to accommodate all of the 1024 transmitting elements and a range of head sizes. For thermal treatments, which are performed at higher frequencies due to the increased absorption in tissue, the steering range is limited. Therefore, for peripheral targets, the head must be translated inside the array [46]. Since the transducers are no longer normally incident to the skull surface, the focal quality deteriorates. Even with corrections employed there is a significant loss of energy at the focus with extreme incident angles [4]. The lower-frequency array which is intended for microbubble-mediated applications has a larger effective steering range. Co-registration between the CT, MRI, and therapeutic coordinates is maintained by inhibiting motion of the head using a stereotactic frame which presents discomfort to the patient, especially for repeat treatments. MRI scans can be carried out prior to each sonication to ensure registration is maintained and to monitor temperature rise. Authors are exploring ways to monitor this temperature rise ultrasonically [47]. For microbubble-mediated procedures however, MRI provides little intraoperative guidance because of the lack of temperature elevation. To maintain skull temperature and facilitate coupling of the ultrasound into the skull, a continuously degassed and cooled water bath is used. Overall, FUS procedures on the brain remain complex and costly, and so are only available in approximately 60 select specialist treatment centres worldwide [48]. For repeated transcranial FUS treatments to be more widely adopted, patient comfort and array designs need to be improved.

In this paper, the concept of a personalised (skull-conformal) transducer array will be introduced that negates the need for a stereotactic frame, water bath, and intraoperative MRI scans. The transducers will be placed at locations to optimise focal parameters at the specific brain target.

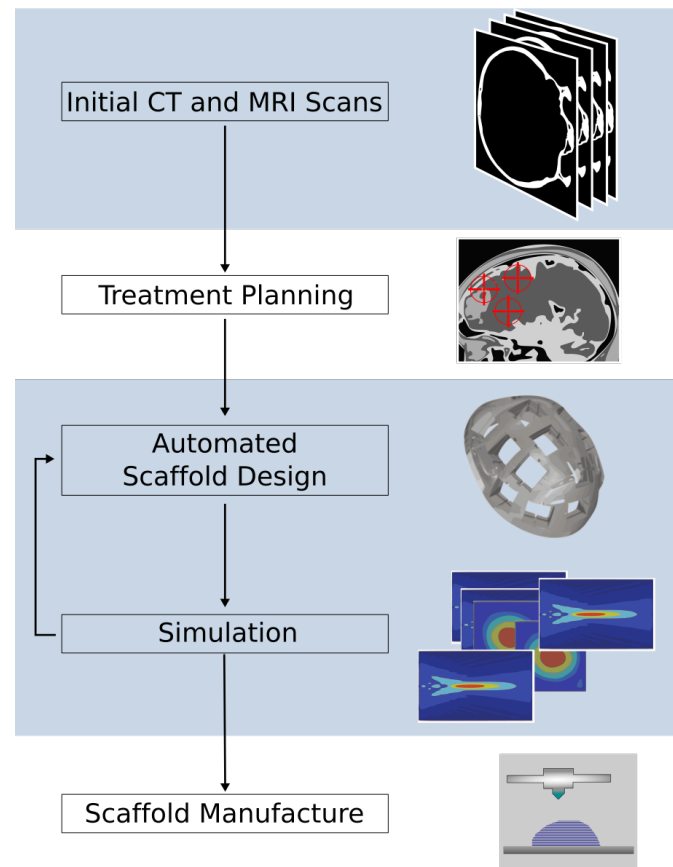


Fig. 1: High-level workflow for the design of a skull-conformal array.

## II. ARRAY DESIGN CONCEPT

It is proposed that motion of the skull relative to the transducers can be inhibited by manufacturing a personalised transducer array for each patient [49]. The array conforms tightly enough to the head surface such that it does not need to be invasively attached, and requires only a thin layer of gel to couple ultrasound from the transducers to the skull surface. The array design may be optimised for each patient’s individual treatment sites.

An overview of the helmet generation process is shown in Fig. 1. The steps are as follows;

- 1) CT and MRI scans of the patient’s head are captured and co-registered. Using the MRI data, treatment planning is then undertaken to generate a list of target coordinates for the focused ultrasound treatment.
- 2) Using simulations, the position of the transducers are then optimised using target locations, coupling efficacy to the skull surface, and ease of array manufacturing. Array designs that are not viable to manufacture (e.g. collision of transducers) are not simulated. This process is automated.
- 3) The optimisation procedure is repeated until a scaffold to house the transducers is produced that best meets the acoustic and manufacturing requirements. The scaffold that conforms tightly to the patient’s scalp is then 3D printed.

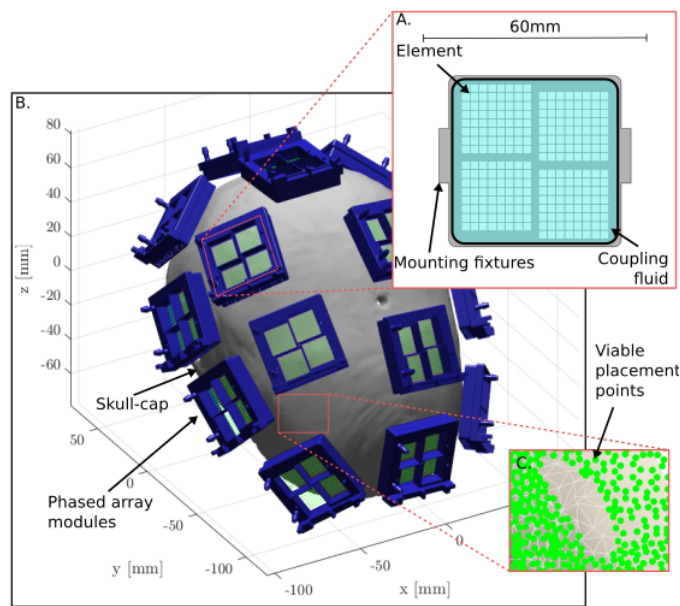


Fig. 2: Optimal conformal array designs for patient-specific targets can be produced using modules. **A.** Example design of a  $2 \times 2$  module. Modules consist of multiple smaller phased arrays. The housing is designed so that modules can be reused and transferred between patients. **B.** Optimal placement on a skull-cap for an arbitrary target. The green dots show the locations of each element in the modules. The removable housing is shown in blue. **C.** Some areas of the skull have a curvature too great to support effective coupling of modules to skull. Valid module placement centres are shown in green.

An early numerical study has already introduced the concept of a skull-conforming array [49], however there are two significant differences between the original design and the design presented here.

The first change is in the transducers used. In the original work it was shown that fixed focus single element transducers, in a conformal configuration could achieve adequate focus throughout the brain. In this work, phased array modules [50], [51] will be used instead as a more practical solution to controlling the sonications.

The second change is in the design of the scaffold. In the original work, the scaffold was designed so as to normally couple as many single element transducers to the skull as possible. However, the flat surface of the phased array designs means that there are patient-specific limitations on placement. Additionally, since there is less overall skull coverage than the fully populated simulation in the original paper, the placement must be optimised. The optimisation process is discussed in greater detail in section III-B.

Fig. 2A shows how the phased array module configuration may be implemented. Each module consists of many individual elements arranged in an  $n \times n$  grid. Cooling and coupling is achieved by circulating continuously de-ionised, de-gassed water around the elements. This allows the transmitting elements to be easily transferred between each patient's helmet and has the advantage of reducing the number of electrical interconnects and thus assembly time. The patient-

TABLE I: Target coordinates used in the simulations. Distances to the skull are the minimum distances from the point to the inner skull surface and are not measured on any particular anatomical plane.

Target no.	Dist. to skull [mm]	Dist. from cent. [mm]
1	14.0	57.8
2	15.9	55.9
3	19.0	68.6
4	38.1	50.0
5	7.9	60.0
6 (centre)	56.4	0

unique rapid-prototyped scaffold is then all that is required to place the transducer elements in the optimal configuration.

### III. NUMERICAL STUDY

In this part of the study, the performance of several conformal array designs were compared to quasi-random hemispherical designs using a finite-difference, *full-wave* simulation [52].

#### A. Finite-Difference Simulation Parameters

An ex vivo human skull cap was previously imaged in a CT scanner (LightSpeed VCT, GE Healthcare, Chalfont St Giles, UK) using the bone plus convolution kernel with an isotropic resolution of  $625 \mu\text{m} \times 625 \mu\text{m} \times 625 \mu\text{m}$ . CT image intensity, acquired in Hounsfield units (HU), was converted to material density using a linear mapping [53]. The skull had a mean density of  $1.68 \text{ g cm}^{-3}$  and a mean thickness of 8.58 mm.

For both conformal and hemispherical designs, a total of 6 targets were considered: five peripheral targets and one central target. Three of the peripheral targets were tightly grouped so as to test the ability of the algorithm to find unique solutions where the search space has few optima. A further two peripheral targets were chosen at random. The distances between peripheral targets and the inner skull surface ranged between 7 and 38 mm. The central target was at the approximate geometric centre of the skull cap. The targets are summarised in Table I and shown graphically in Fig. 3

Although larger than the frequency used for clinical BBB treatments, both hemispherical and conformal array designs were modelled at a frequency of 520 kHz which is close to that used clinically in thermal treatments (620–720 kHz) as it matched the availability of transducers at the time of subsequent experiments. The speed of sound and attenuation in the skull was interpolated from experimental measurements [19]. The skull cap was discretised at  $\lambda/10$  in water. Temporal discretisation was  $\text{CFL} = 0.1$ . For modelling the transducers, the Neumann boundary condition (NBC) was used. The transducer surfaces were modelled with reflective backing enforced by setting the  $\text{NBC} = 0$ , creating a set of voxels that represent the transducer surface and another set immediately behind it which were reflective.

Although the full volume was simulated, a smaller volume centered around the target that was 16 mm in length, width and depth was considered for assessing focal quality. PSRLR (peak sidelobe ratio, the ratio of the largest maxima outside the focus to the peak pressure at the focus) and focal volume

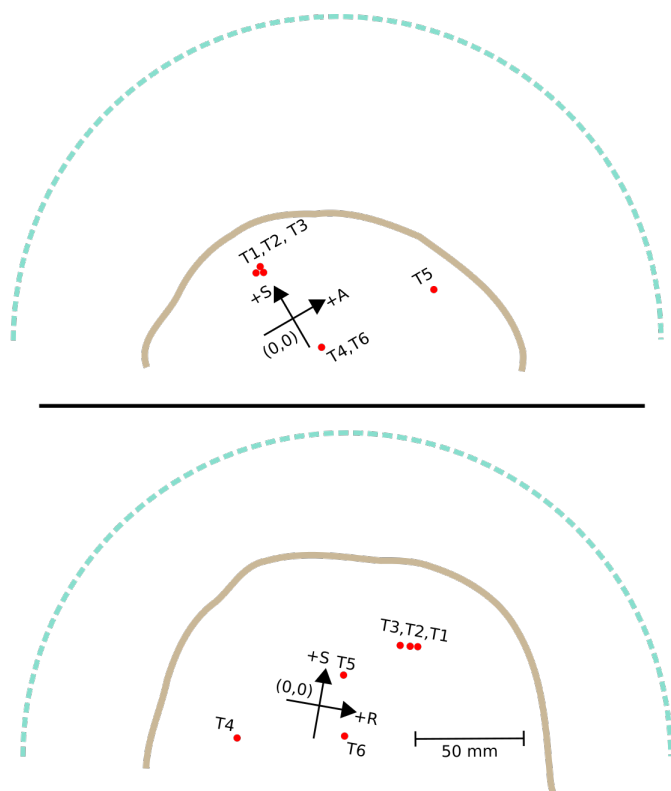


Fig. 3: Locations of the targets used for the simulations in terms of CT co-ordinates from two anatomical planes. The inner skull surface is shown. Diagram is to scale. **Top:** Sagittal plane **Bottom:** Coronal plane. The blue dashed lines represent the arc on which the hemispherical transducers were placed for the hemispherical array. The planes shown here have no bearing on the measured distances from point to the skull. Distances between the points and the inner skull surface are the shortest distance and do not necessarily lie on any anatomical plane.

were computed. PSLR was found using multi-dimensional differentiation [54]. The focal volume was found by computing the number of voxels in the 3D dataset greater than -6 dB. Additionally, focal gain ( $P_i/P_o$ ) which can provide an estimate of skull heating was found by computing the maximum pressure within the assessment volume ( $P_i$ ) and maximum pressure outside of the skull ( $P_o$ ).

### B. Conformal Array Design Procedure

A maximum of 4096 elements (surface area permitting) were used in the conformal array simulations, but two different configurations of the modules were considered. In both configurations, elements were first grouped into 64 element square phased arrays. In the first configuration, modules consisted of only one of these phased arrays ( $1 \times 1$  grid). In the second configuration, modules were formed from a  $2 \times 2$  grid of these phased arrays. The two configurations are summarised in Table II. The size of the module housing reduces the number of unique placement opportunities for individual elements. Subsequently, to interrupt the spatial periodicity of the array, for the  $2 \times 2$  modules, an offset grid was used as shown

TABLE II: The distribution of elements into modules for the two simulation configurations of the conformal array.

Configuration	$1 \times 1$	$2 \times 2$
Maximum possible elements	4096	4096
Elements in each sub-module	64	64
Sub-modules in each module	1	4
Elements in each module	64	256

in Fig. 2A. Overall this increases the randomness of the element placement in a case where whole modules are very close together. An advantage of the  $2 \times 2$  configuration is the reduced number of interconnects, but there are less placement opportunities compared to the  $1 \times 1$  configuration. In either case, the pitch of each 64 element array was 1.50 mm and the width of each element was 1.43 mm.

For each target, a unique conformal array was designed. Since a typical skull cap surface comprises many thousands of placement options for modules, it was necessary to quickly simulate numerous designs during array optimisation. To reduce simulation time, although less accurate, a *ray-acoustics* (RA) approach, updated to include shear wave propagation [55], [56], was favoured over a finite-difference approach [57]. For large volume transcranial simulations, ray acoustics is between 500 to 1000 times faster than classical finite-difference simulations, although the speed-up depends on a large number of factors. The ray propagation simulation technique accounts for reflection of sound entering the skull, and refraction of longitudinal and shear waves. Ray acoustics was used only for the scaffold conformal array design procedure. For comparing the hemispherical and optimised conformal arrays, the previously described full-wave approach was used. It was not sufficient to use ray acoustics to compare the two array types, as reflections from the inside of the skull were not included in the RA model so as to achieve maximum simulation speed. The ray acoustics took approximately 100 seconds to compute on a single GPU (GeForce GTX TITAN X, Nvidia, USA), whilst the full-wave simulations took approximately 12 hours to compute on 24 threads on Sunnybrook's cluster (Xeon, Intel, USA).

To design the array, inner- and outer-skull meshes were first generated from the CT-density images by thresholding and discretising using a total of  $60 \times 10^3$  polygons, which equates to approximately 1 point per  $3 \text{ mm}^2$ . The centre of gravity of each triangle in the outer-skull mesh were considered as possible placement centres for modules. Binarised coupling efficacy was determined for every triangle in the outer skull mesh. Nearby (based on the size of the module) triangles were used for the computation of an area-weighted normal. A plane was formed from the area-weighted normal axis and the outer points on the skull mesh. If this plane was greater than 5 mm from any of the triangles, the origin point was discounted. Given the mesh size and the skull cap used, this resulted in approximately 25000 possible locations for modules to be placed. Fig. 2C shows a section of the outer skull mesh and its valid placement locations (green dots). From the figure it can be seen that there is an absence of valid points on an area of high curvature of the skull which would result in ineffective coupling.

For optimisation, all modules were first manually placed so

as to maximise coverage of the skull cap, forming an initial configuration. Given the extremely large number of possible configurations ( $\approx 25000^{16}$ ) and high dimensionality of the problem, it was not feasible to use traditional optimisation techniques. Therefore, a randomised approach was taken to optimisation.

For each iteration in the optimisation algorithm, the modules were translated a small random distance from the initial location such that the resulting configuration was still realisable, i.e. no interference between modules. Enlarged bounding boxes were added to the modules in the algorithm to ensure that there was sufficient room for interconnects and mounting hardware. Every configuration was assessed using a GPU-accelerated (GeForce GTX TITAN X, NVIDIA, USA) implementation of the ray-acoustics simulator. Simulations were done by first reverse propagating ultrasound from the target to the transmitters to calculate phases and then run forward to obtain the pressure field. The PSLR was recorded for every iteration considered. The design with the lowest PSLR at the end of the optimisation procedure was considered to be the most optimal design. For this study, 50% PSLR was set to be the maximum acceptable limit for a design that would achieve safe targeting in practice.

For every target and both module configurations, 200 iterations were considered by the algorithm. Each iteration took about 150 seconds to compute. An example of an optimised configuration for  $2 \times 2$  modules is illustrated in Fig. 2B. The green dots show the centres of each element and the blue volume represents the bounded volume included to allow for interconnect and cooling. Given that a skull cap has a limited area compared to a full skull, only 60 modules in the  $1 \times 1$  and 16 in the  $2 \times 2$  configuration could be placed on the skull surface.

### C. Hemispherical Array Designs

Two different hemispherical arrays were simulated, which were modeled using circular piston transducers distributed on a 30 cm diameter hemispherical shell. Placement of the modules was computed using a quasi-random Fibonacci spiral algorithm to approximate even spatial coverage [58]. One hemispherical array had an equivalent element density to the conformal array (element number = 3840; element diameter = 1.35 mm), whereas the other had an equivalent element density to the existing clinical transcranial FUS brain system (element number = 1024; element diameter = 10 mm) [59], [60].

## IV. EXPERIMENTAL STUDIES

Based on the results from the numerical simulations, a conformal phased array was designed for testing with an ex vivo human skullcap. The array was constructed, characterized acoustically via benchtop experiments, and employed in a preliminary in vivo study of BBB opening in rodents.

### A. System Design and Acoustic Characterization

For the experimental studies, the optimisation procedure (described in the previous section) was run for 200 iterations

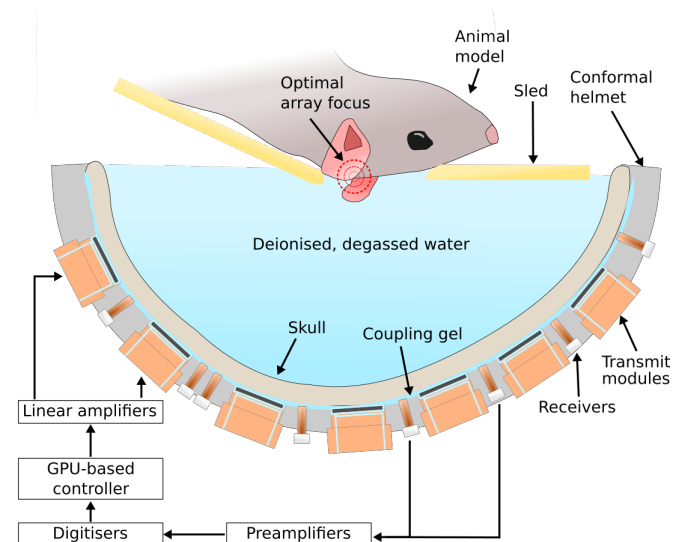


Fig. 4: Experimental configuration for the in vivo experiments.

to produce a helmet design. The helmet was designed for optimal focus (lowest PSLR) in the centre of the skull in the transverse and coronal planes, and at the bottom of the skull in the sagittal plane which is depicted as *optimal array focus* in Fig. 4 (approximately at the base of the temporal lobe). For the experiments, only the  $2 \times 2$  modules were used, due to their availability at the time of the experiment. The scaffold and module housings were 3D printed (3D Systems Inc., USA). The centre frequency of the elements was 520 kHz. Each element was driven by a miniature linear amplifier and waveform generator developed in house, which facilitated both programmable phase and amplitude [61]. The resolution of the transmit pressure for the phased array was 11 bits. The helmet was split into two halves so that it could be quickly attached and removed from the skull. Retention of the two halves was maintained with a bespoke cam mechanism.

A sparse receiver array was added to the FUS system for acoustic monitoring and control purposes [62]–[65]. The receiver array consisted of 64 air-backed piezoceramic cylindrical elements, 3 mm in diameter, with center frequencies tuned to the subharmonic of the transmit array (260 kHz). Harmonic emissions [66], [67] have been identified as a possible indicator of treatment outcome. Compared to other harmonics, subharmonic and ultraharmonic emissions can only arise from bubble emissions and are an indicator of stable cavitation [68]. One advantage of using the subharmonic as opposed to ultraharmonics is the reduced attenuation through skull.

Fixed gain pre-amplifiers (40 dB) were added to the receive lines, and the signals were digitised using four 16-channel data acquisition cards (ATS9416; AlazarTech, QC, Canada). The receivers were populated randomly within the helmet scaffold in the vacant space separating transmit modules, and their locations were confirmed via acoustic triangulation using a narrowband fixed source (piezoceramic tube; 1 mm diameter, 5 mm length, 0.5 MHz center frequency).

Prior to each experiment, the ex vivo human skullcap was degassed in a vacuum jar (Nalge, Rochester, NY, USA; Gast,

Benton Harbor, MI, USA) at  $-0.1$  MPa for a minimum of 2 h. The FUS system was assembled by inserting the transmit modules and receiver elements into the two halves of the helmet scaffold. Following insertion, an ultrasound gel was liberally applied to the interior surface of the scaffold to provide acoustic coupling, and the two halves of the helmet were placed flush with the skullcap and secured together. A thin plastic membrane was placed between the skullcap and the helmet scaffold, which was filled with (degassed & deionised) water (Fig. 4). Where possible, coupling was ensured by visually inspecting the gel through the clear plastic membrane.

Acoustic characterization of the conformal phased array was performed using a fibre-optic hydrophone ( $10\ \mu\text{m}$  active tip diameter, Precision Acoustics, Dorchester, Dorset, UK) mounted to a 3D positioning system (Velmex, USA). Three-dimensional trans-skull pressure field measurements (field-of-view (FOV) =  $8\ \text{mm} \times 8\ \text{mm} \times 8\ \text{mm}$ ; voxel size =  $0.25\ \text{mm} \times 0.25\ \text{mm} \times 0.25\ \text{mm}$ ) were acquired from optimised and unoptimised helmet configurations, both with and without full-wave simulation-based transcranial phase aberration corrections [52]. Ellipsoids were fit to the resulting 3D pressure field distributions, and 2D maximum-intensity projected planar field plots were generated based on the orientation of the three major axes.

### B. In Vivo Experiments

Four Sprague Dawley rats (male,  $\approx 0.3$  kg; Charles River, Canada; Taconic, Canada) were used to test the system in vivo. All experiments were performed with prior approval from the Animal Care Committee at Sunnybrook Research Institute (SRI) and were in accordance with the Canadian Council on Animal Care and ARRIVE (Animal Research: Reporting of In Vivo Experiments) guidelines. Animals were anaesthetised via intraperitoneal injection of a mixture of ketamine ( $50\ \text{mg/kg/h}$ ) and xylazine ( $5\ \text{mg/kg}$ ). To remove possible cavitation nucleation sites and maximise coupling into the animal brain, hair on the animals' heads was removed using an electric razor and depilatory cream. The scalp was washed with mild soap and water to prevent chemical irritation from the cream. The tail vein was catheterised using a 25G angiocatheter. The animals were laid supine on a sled with a cutout to enable acoustic coupling of the head with the FUS system (Fig. 4). The animals were positioned such that the mid-brain region was within 1 cm from the intracranial target location for which the phased array was optimized. Body temperature was maintained using blankets and heated saline packs. Animals were sacrificed immediately after the experiment.

The FUS procedures were performed under MRI guidance at 3.0 T (Biograph mMR; Siemens Healthcare, Erlangen, Germany). All FUS exposures were performed outside of the MRI suite, as the FUS system employed was not MRI compatible. Co-registration between the MRI and FUS system coordinates was obtained using three narrowband fixed sources (Piezoceramic tube; 1.2 mm diameter, 256 kHz center frequency) attached to the sled. The central locations of the fixed sources were first determined in MRI coordinates using 3-plane localizer scans. The sled was then reattached to the

FUS system and the sources were excited sequentially with an impulse from a pulser (Panametrics, Olympus-NDT, Inc., Waltham, MA, USA). Their spatial coordinates with respect to the array were determined via triangulation. From the triangulated coordinates and the measured MR coordinates, a transformation matrix was constructed to convert between MR and therapeutic coordinates and vice versa.

MR images were acquired (7 cm diameter loop coil) using a T2-weighted (T2w) sequence for target selection (turbo spin echo; repetition time: 3100 ms; echo time: 80 ms; number of averages: 4; echo train length: 8; matrix size:  $128 \times 128$ ; field of view:  $7 \times 7\ \text{cm}$ ; slice thickness: 1.5 mm), a T1-weighted (T1w) sequence before and after intravenous injection of a gadolinium-based MRI contrast agent (0.1 mL/kg Gadovist; Bayer Inc., Toronto, ON, Canada) to detect BBB opening (turbo spin echo; repetition time: 500 ms; echo time: 7 ms; number of averages: 3; echo train length: 4; matrix size:  $128 \times 128$ ; field of view:  $8 \times 8\ \text{cm}$ ; slice thickness: 1.5 mm), and a T2\*-weighted (T2\*w) sequence to monitor for red blood cell (RBC) extravasations produced by the sonications (3D gradient echo; repetition time: 27 ms; echo time: 15 ms; number of averages: 4; echo train length: 1; matrix size:  $128 \times 128 \times 16$ ; field of view:  $7 \times 7 \times 2.4\ \text{cm}$ ; slice thickness: 1.5 mm). A comprehensive set of MR images (i.e., T1w/T2w/T2\*w scans) was acquired before and approximately 10 minutes after each FUS treatment.

Pulsed FUS exposures (frequency: 520 kHz, pulse length: 10 ms, PRF: 1 Hz) were applied in combination with an intravenous injection ( $20\ \mu\text{l/kg}$ ) of contrast agent microbubbles (Definity microbubbles; Lantheus Medical Imaging, North Billerica, MA, USA). The microbubbles were diluted in normal saline and infused through the tail vein catheter over 60 s, beginning simultaneously with the start of each sonication. Starting from an estimated focal pressure of 0.1–0.2 MPa in situ, the applied pressure level was increased from pulse-to-pulse (step size  $\approx 10$ – $20\ \text{kPa}$ ) until spatially-coherent subharmonic microbubble activity was detected near the intended target using 3D acoustic imaging.

For the 3D imaging, the receiver signals from each pulse were bandpass filtered (fourth-order Butterworth filter, 250–270 kHz passband) and reconstructed over a 3D volume centered on the intended target (field-of-view (FOV) =  $10\ \text{mm} \times 10\ \text{mm} \times 14\ \text{mm}$ ; voxel size =  $1\ \text{mm} \times 1\ \text{mm} \times 1\ \text{mm}$ ) on a GPU (GeForce GTX 1080) using a delay, sum, and integrate beamforming algorithm [63], [69].

Following detection of subharmonic microbubble activity, the applied pressure was reduced to 50% of the value required to achieve detection. This pressure was maintained for the remainder of the sonication (frequency: 520 kHz, pulse length: 10 ms, PRF: 1 Hz, duration: 120 s). This approach has been shown previously to increase BBB permeability without causing overt tissue damage [64], [70]. In the first three animals multiple successive single point exposures were applied, and in the fourth animal a single multi-point exposure ( $2 \times 2$  point grid, 2 mm point spacing) was tested. For the multi-point exposure, the applied pressure was calibrated independently at each target location [65].

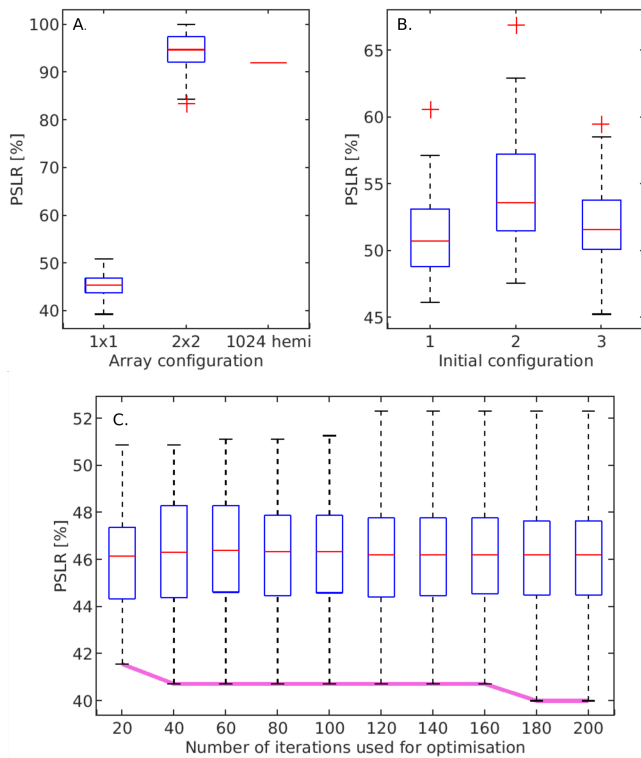


Fig. 5: Statistical summary of the PSLR obtained from 200 iterations of the optimisation algorithm. Different module configurations and targets are shown. Optimisation results obtained when using both  $2 \times 2$  and  $1 \times 1$  configurations are shown. **A.** Optimisation for peripheral target 1 (57.8 mm from the geometric centre). As a reference, the 1024-element hemispherical system is shown, but there is only one observation since the array design is fixed. **B.** Optimisation for the central target with a  $2 \times 2$  configuration, but seeding the algorithm with three different initial placements. The design with the lowest PSLR was considered optimal in each case. **C.** Optimisation of a peripheral target using an increasing number of iterations. The pink line tracks the performance of the best design as the number of iterations is increased

## V. RESULTS

Fig. 5 shows a statistical summary of results from the optimisation algorithm. After 200 iterations of the optimisation algorithm it was not possible to generate a helmet for target 1 using a  $2 \times 2$  module configuration with satisfactory performance (Fig. 5, left,  $\text{PSLR}_{\min} \approx 80\%$ ). The results were similar for close-by targets 2 and 3 as well (not shown), which on average had a best case PSLR of 87%. However, using a  $1 \times 1$  arrangement, an optimal configuration with acceptable PSLR was found for target 1. The optimal design exceeded the performance (in terms of PSLR) of the 1024-element hemispherical array. For target 1, the range of results for the  $1 \times 1$  configuration was 39%–51%, 92% for the 1024-element hemispherical, and 84%–99% for the  $2 \times 2$  configuration. The data also shows (Fig. 5B) that the initial placement configuration has a role in the minimum PSLR that can be achieved through optimisation (45%–48%).

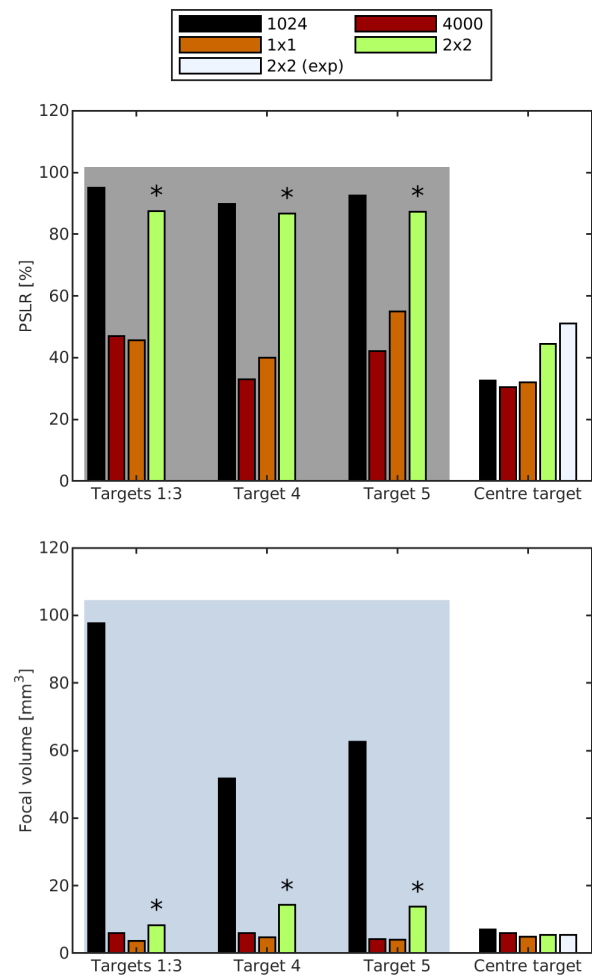


Fig. 6: The performance of the optimised helmets and the two hemispherical layouts for 6 different targets. Experimental results of the  $2 \times 2$  configuration, target 6 are included for comparison. Peripheral targets are highlighted by the gray box. Targets 1–3 were tightly grouped, so were averaged. **Top:** Ratio of sidelobe to target pressure (PSLR). **Bottom:** The -6dB focal volume. The values were obtained using a finite difference model, except those labelled with a \* which were calculated using ray acoustics.

Fig. 6 compares the performance of the optimised conformal arrays in both module configurations ( $1 \times 1$  and  $2 \times 2$ ) with both configurations of the hemispherical array (equivalent total elements and clinical-density). For targets 1–5, the performance of the  $2 \times 2$  designs did not warrant the additional verification by full-wave simulation, as the PSLR in these cases was above or at the 50% maximum limit described in the method. However, for completeness, approximations using ray-acoustics have been included and are labelled with a \*. The range of volumes over the closely group targets 1–3 was between  $76.7 \text{ mm}^3$ – $115.0 \text{ mm}^3$  for the 1024-element hemispherical array,  $5.9 \text{ mm}^3$ – $5.9 \text{ mm}^3$  for the 4000-element hemispherical array,  $3.5 \text{ mm}^3$ – $3.7 \text{ mm}^3$  for the  $1 \times 1$  conformal array and  $7.2 \text{ mm}^3$ – $10.9 \text{ mm}^3$  for the  $2 \times 2$  configuration. For

targets 1–3, there was also an improvement in PSLR when using a  $1 \times 1$  conformal configuration. The range of sidelobes for these targets was as follows, 93%–98% for the 1024-element and 46%–47% for the 4000-element hemispherical arrays, 44%–48% for the  $1 \times 1$  conformal array, and 87%–89% for the  $2 \times 2$  configuration.

The performance of the arrays for the central target were comparable across the array configurations, with the central-target-optimised  $2 \times 2$  configuration performing worst in terms of PSLR and the 1024-element array worst in terms of focal volume. The manufactured helmet ( $2 \times 2$  configuration, central target) had a PSLR of 44% in simulation and a focal volume of  $4.9 \text{ mm}^3$ . When this array design was tested experimentally (Fig. 6), at 50% the PSLR was marginally higher (+6%), as was the focal volume of  $5.5 \text{ mm}^3$  (+11%).

Compared to full-wave, the ray acoustics approach is well-suited for the optimisation procedure due to its fast execution speed, however it is less accurate than full wave. Post-hoc comparison of the RA, full-wave and experimental data was conducted. Ray acoustics underestimated the PSLR by a maximum of 6% ( $1 \times 1$  configuration, target 1) and overestimated by a maximum of 1%. For the peripheral targets (1–3) the RA underestimated the PSLR by 5% on average, and overestimated by 1% for the other targets (4–6). The error between full-wave simulations and experimentally measured sidelobe ( $2 \times 2$ , target 6) was 2%.

The results labeled simulation in Fig. 7 compare the simulated peak negative pressure profiles obtained using the clinical-density hemispherical array and both arrangements,  $2 \times 2$  (which was ultimately manufactured), and  $1 \times 1$  of the conformal array. The results labeled experiment in Fig. 7 show the experimentally obtained negative pressure profiles from helmets constructed with a  $2 \times 2$  configuration. The defocusing effect of the skull is apparent from the presence of several off-target lobes when the helmet was unoptimised and no corrections were applied. Applying skull corrections reduces the presence of these lobes significantly, but prominent grating lobes with a 65% amplitude persist. These lobes were suppressed further when an optimised helmet in conjunction with skull corrections was used, reducing the PSLR to 51%.

Fig. 8 shows select computed focal gains for the 1024-element hemispherical array and two configurations of the conformal arrays in their optimal configuration. The 1024-element hemispherical design had the best performance for the central target  $P_i/P_o = 6.16$  and targets 1–3 (0.583–0.587) but did not perform as well as the  $1 \times 1$  conformal array for targets 4 and 5. Low focal gain contributes to skull heating in thermal treatments. However since the conformal array designs are intended predominately for non-thermal treatments, where the duty cycles are considerably lower, focal gain was not made the objective of the optimisation algorithm. Whilst low focal gain does increase the risk of skin burns from heating of the transducers, temperature measurements of the transducers ( $N = 8$ ) near the surface of the skull were not found to exceed  $33^\circ\text{C}$  over the 120 s sonication. Focal gain could be included in the optimisation algorithm if treatments utilising an increased duty cycle were required. It is expected that loss of energy through the skull could be reduced by placing transducers in

a way as to reduce highly attenuating shear wave propagation.

Fig. 9 shows representative MRI data acquired following single point and multi-point FUS exposures. There was successful BBB opening in all 4 of the rats used in the experiments. However, in one of the animals, the opened volume was approximately twice the expected volume, due to incorrect controller parameters, but on target. Opening was consistently on target ( $\pm 1 \text{ mm}$ ). The controller triggered at pressures between approximately 0.62 and 0.73 MPa, which corresponded to treatment pressures between 0.31 and 0.37 MPa. There was no evidence of hemorrhage or edema from the T2\*w images (Fig. 9, right) in any of the animals. In three of the animals there was opening near the skull, due to reflections and targets being placed close to the rat skull. This result is not expected in larger animals or humans. In all animals contrast was enhanced in the sinuses and the cerebellum (Fig. 9, centre).

Fig. 10 shows examples of passive acoustic mapping of spatially-coherent bubble emissions from one of the animals. Fig. 10A shows an increase in the noise floor due to the large transmit pressure, but no spatially coherent emissions. Fig. 10B shows spatially coherent emissions which triggered the controller. Fig. 10C shows that the noise floor reduces significantly at the start of the treatment cycle following a reduction in the transmit pressure.

## VI. DISCUSSION

We demonstrated the feasibility of using a new method to manufacture personalised transducer arrays. The arrays are targeted at transcranial focused ultrasound blood-brain barrier treatments, and we were able to automatically optimise the array design for specific treatment sites. Simulation results showed that optimised array PSLR performance exceeded that of the 1024-element hemispherical array and that the focal volume was consistently smaller which facilitates more precise targeting. However, the poor performance of the 1024-element hemispherical array is thought to be caused by the size of the elements. This particular array with large element sizes like those in the Insightec clinical system is designed to maximise energy deposition preferentially at the centre of the array, which is evidenced by the high focal gain at the central target. Likewise, the marginal differences between the 4000-element hemispherical and  $1 \times 1$  conformal arrays are perhaps due to element size and skull coverage, which warrants further study in subsequent work. These marginal improvements in focal volume could be due to reduced shear wave propagation, but this cannot be confirmed with the accuracy of shear wave modelling used. However, the main advantage of the conformal configurations is the co-registration of the treatment and imaging coordinate systems which was maintained by a 3D printed scaffold that conformed tightly to the skull. This has the benefit of not requiring a continuous circulation of degassed and cooled water or an uncomfortable stereotactic frame.

The manufactured array was used to safely modulate the permeability of the BBB in a rat model. The transmit pressure and phase resolution of the system was sufficient to overcome

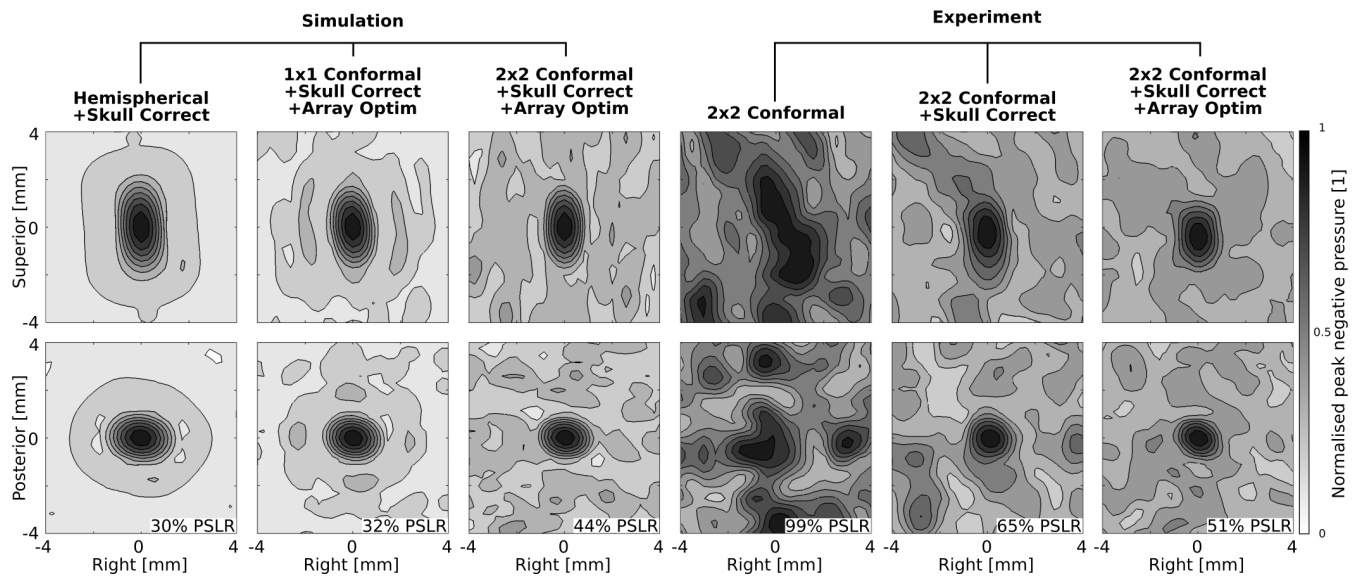


Fig. 7: Comparison of maximum-intensity-projected pressure profiles obtained from experiments and from simulations. All results were captured at the same location relative to the skull with equivalent sources. In each configuration and plane, results are self-normalised. Each contour represents a 10% step in pressure, so that white represents 0–10% and black represents 100%. The left three columns are trans-skull simulation results obtained using a full-wave finite difference simulation using two configurations of the conformal array ( $1 \times 1$  and  $2 \times 2$ ) as well as a clinically-relevant 1024-element hemispherical design. The right three columns show experimentally obtained data from two  $2 \times 2$  conformal configurations; (1) an unoptimised helmet with no aberration corrections, (2) the same helmet but with aberration corrections and (3) the optimised helmet used in the in vivo experiments also with aberration corrections applied. Two dimensional cubic interpolation was applied to reduce voxelisation of the experimental images.

the attenuation and phase aberrations of a human skull cap. In some cases there was excessive opening which can be attributed to poorly optimised controller settings at the time of the experiment.

Automated design of a helmet takes approximately 6 hours, with each iteration of the optimisation algorithm taking 100–150 s. Improvements in speed via optimised simulation algorithms are being explored. The results show that testing randomised configurations is effective in finding more optimum array designs. Following optimisation, helmet manufacture takes approximately 12 hours. The tolerance between the skull and element positions for effective coupling has been found heuristically and may need to be adjusted to accommodate a scalp in a clinical setting. For a clinical system it may be necessary to implement additional acoustic controls to ensure effective coupling between transmitters and skull, as the quality of the focus may be affected by the quality of the coupling. The scaffold provides an opportunity to include transducers to localise and verify effective coupling with the skull [71].

Skull caps provide a significantly reduced area to place transducers and it is expected that the additional area offered from a full skull may further improve focal volume and steering opportunities since more modules can be placed. The role of initial placement configuration in minimum PSLR is expected to be negligent experimentally (45%–48%). The narrow range of the optimisation results imply that the targets were not inadvertently chosen to be some natural optima and that the optimisation algorithm was effective at producing

unique designs for each treatment site with a low PSLR. The optimal designs for the closely grouped near-skull targets were unique.

Two module configurations were considered for the arrays,  $2 \times 2$  and  $1 \times 1$ , with the former being preferred for its reduced assembly time. The greater flexibility in placement of  $1 \times 1$  modules awarded better performance than a  $2 \times 2$  configuration. Conversely, the poor performance of the  $2 \times 2$  module designs was likely due to the poor focal gain that arose from constraints on placing the modules in close proximity. For this reason, it was not deemed necessary to obtain performance metrics for targets 1–5 (Fig. 6) using full wave simulations, since no designs with satisfactory performance (as defined by the PSLR criteria in the method) could be produced. However, for the central target it was possible to design an array using  $2 \times 2$  modules with an adequately low PSLR (44%) for treatment. This array was the only one tested experimentally. For peripheral targets, the  $2 \times 2$  design is expected to perform worse than the 1024-element hemispherical design based on simulations, but the  $1 \times 1$  design should be equal or better. Future experimental studies are needed to validate this for the  $1 \times 1$  design, especially for peripheral targets. Although overall the performance in terms of PSLR was not as good as the hemispherical layouts for the central target (30%), a  $2 \times 2$  module configuration may be worth pursuing for centrally located treatment sites given the other practical advantages.

Element count did not appear to be a major contributor to the focal volume. The  $2 \times 2$  configuration had the most number of elements (4096), but was consistently the worst performing.

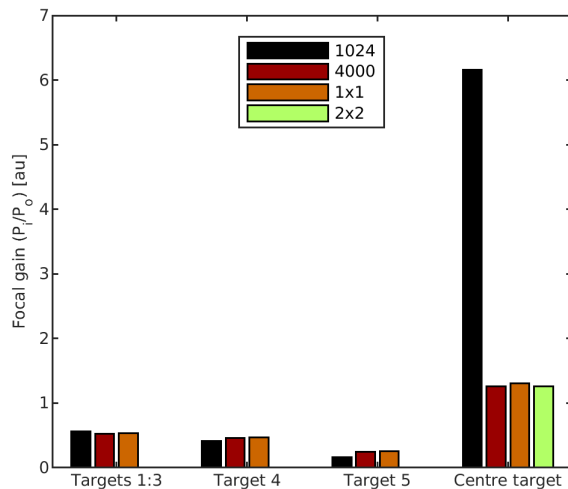


Fig. 8: Focal gains computed using full-wave simulations for all six targets and select array configurations. No data for the  $2 \times 2$  configuration, targets 1–5 was available since RA simulations demonstrated that no design with satisfactory performance could be produced ( $PSLR > 50\%$ ).

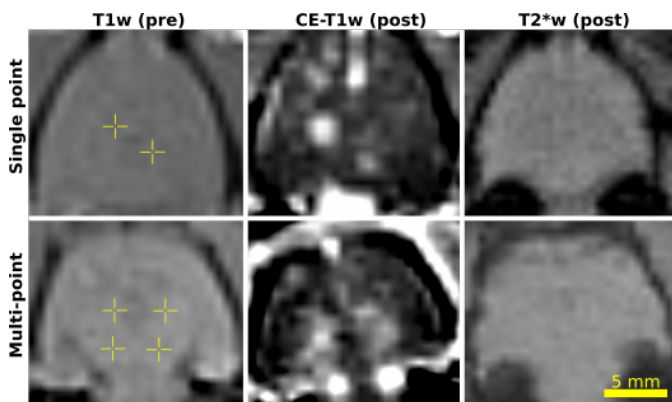


Fig. 9: Examples of MR images captured during the in vivo experiments. The T1w images were taken before treatment. T1w(post) and T2\*w were taken after. The top row of images correspond to a two point exposure. The bottom row of images correspond to a multi-point  $2 \times 2$  exposure. The yellow reticles indicate the target sites. The contrast windowing selected was self-normalised so as to maximise contrast in each image.

The  $1 \times 1$  configurations used a total of 3840 elements, but had smaller volumes across all targets than the hemispherical arrays, even when the same number of elements were used. The 4000-element hemispherical array greatly outperformed its 1024-element counterpart, but as already discussed, this is likely the result of the reduced directivity of the smaller sources rather than purely element count.

With the array and sonication parameters used, heating of the skull from acoustic absorption is not likely. Although the device is not targeted at thermal treatments, future work should consider the impact of a conformal approach on time averaged intensity.

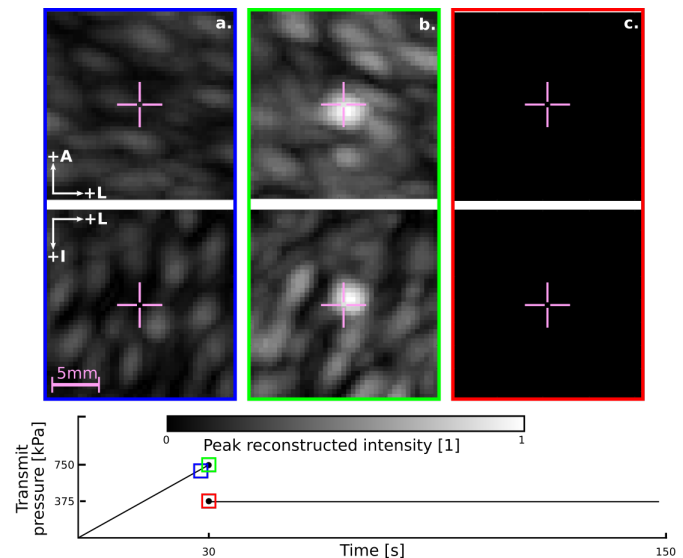


Fig. 10: The results from passive acoustic mapping at three different stages during the calibration and treatment cycle; from the ramp phase immediately before the detection of spatially coherent subharmonic emissions (a), the first and only sonication where there was a detection (b) and during the treatment phase after the acoustic pressure has been reduced to 50% (c). The images are maximum intensity projections onto the sagittal (top) and coronal planes (bottom) from a  $20 \times 20 \times 20$  mm volume. All images are normalised to the same scale. The pink reticle marks the targeted co-ordinates.

The normalised negative pressure plots obtained from simulation (Fig. 7) show lobes appearing as several concentric rings for the hemispherical configuration, although this may differ for the clinical system, as the exact positions of the elements are slightly different from ones used in the simulation. The element positions of the conformal  $2 \times 2$  creates one concentric sidelobe around the main focus, with the rest of the field being highly disrupted. There is also slight counter-clockwise rotation of focus in the sagittal plane from hemispherical to conformal. The focus using the conformal configuration is marginally smaller. Overall, the images show that the conformal array can achieve adequate focusing for BBB treatments with the distribution of pressure that is comparable to the hemispherical array, and PSLRs less than 50%. Between simulations and experiment there was a 7% increase in PSLR. Although an 8 mm cubed volume (16 mm in simulations) was used for assessment of focal volume, coarse three dimensional scans (not shown), and post-hoc analysis of the simulations did not detect the presence of any significant ( $> 5\%$  of focus pressure) lobes outside of this volume.

## VII. CONCLUSION

In this study, we demonstrated the first implementation of a skull-conformal phased array for transcranial FUS therapy. In the proposed approach, patient-specific helmet scaffolds are designed using algorithms based on CT and MRI neuroimaging data, with multi-element transducer modules placed in optimal configurations for the treatment location(s) of inter-

est. Conformal array designs were compared with traditional hemispherical arrays via computer simulations of trans-skull ultrasound propagation. The numerical results showed that conformal and hemispherical arrays provided similar focal quality at central targets, whereas at peripheral targets conformal arrays produced significantly lower focal volumes. A 4096-element skull-conformal phased array was manufactured for experimental testing with an ex vivo human skullcap. Acoustic field measurements confirmed the system's ability to focus through human skull bone via transcranial phase aberration corrections, and a preliminary in vivo study demonstrated safe trans-human skull BBB opening in rodents. Skull-conformal arrays have the potential to improve patient comfort and reduce treatment costs, thereby accelerating the adoption of transcranial FUS therapy.

#### ACKNOWLEDGMENT

The authors would like to thank Shawna Rideout-Gros and Viva Chan for assistance with the animal experiments.

#### REFERENCES

- [1] C. J. Diederich and K. Hynynen, "Ultrasound technology for hyperthermia," *Ultrasound in medicine & biology*, vol. 25, no. 6, pp. 871–887, 1999.
- [2] G. Ter Haar, "Ultrasound focal beam surgery," *Ultrasound in medicine & biology*, vol. 21, no. 9, pp. 1089–1100, 1995.
- [3] M. Lee *et al.*, "Thermal dose and radiation dose comparison based on cell survival," *Journal of Therapeutic Ultrasound*, vol. 3, no. 1, P26, 2015.
- [4] N. McDannold *et al.*, "Transcranial magnetic resonance imaging-guided focused ultrasound surgery of brain tumors: Initial findings in 3 patients," *Neurosurgery*, vol. 66, no. 2, pp. 323–332, 2010.
- [5] W. J. Elias *et al.*, "A randomized trial of focused ultrasound thalamotomy for essential tremor," *New England Journal of Medicine*, vol. 375, no. 8, pp. 730–739, 2016.
- [6] A. E. Bond *et al.*, "Safety and efficacy of focused ultrasound thalamotomy for patients with medication-refractory, tremor-dominant parkinson disease: A randomized clinical trial," *JAMA neurology*, vol. 74, no. 12, pp. 1412–1418, 2017.
- [7] W. S. Chang *et al.*, "Unilateral magnetic resonance guided focused ultrasound thalamotomy for essential tremor: Practices and clinicoradiological outcomes," *J Neurol Neurosurg Psychiatry*, vol. 86, no. 3, pp. 257–264, 2015.
- [8] M. Kim *et al.*, "Treatment of major depressive disorder via magnetic resonance-guided focused ultrasound surgery," *Biological psychiatry*, vol. 83, no. 1, e17–e18, 2018.
- [9] J. Ophir and K. J. Parker, "Contrast agents in diagnostic ultrasound," *Ultrasound in medicine & biology*, vol. 15, no. 4, pp. 319–333, 1989.
- [10] D. E. Goertz, "An overview of the influence of therapeutic ultrasound exposures on the vasculature: High intensity ultrasound and microbubble-mediated bioeffects," *International Journal of Hyperthermia*, vol. 31, no. 2, pp. 134–144, 2015.
- [11] D. McMahon *et al.*, "Increasing BBB permeability via focused ultrasound: Current methods in preclinical research," *Blood-Brain Barrier*, vol. 26, pp. 267–297, 2019.
- [12] T. Mainprize *et al.*, "Blood-brain barrier opening in primary brain tumors with non-invasive MR-guided focused ultrasound: A clinical safety and feasibility study," *Scientific reports*, vol. 9, no. 1, pp. 1–7, 2019.
- [13] S. H. Park *et al.*, "Safety and feasibility of multiple blood-brain barrier disruptions for the treatment of glioblastoma in patients undergoing standard adjuvant chemotherapy," *Journal of Neurosurgery*, vol. 1, no. aop, pp. 1–9, 2020.
- [14] N. Lipsman *et al.*, "Blood-brain barrier opening in alzheimers disease using MR-guided focused ultrasound," *Nature communications*, vol. 9, no. 1, pp. 1–8, 2018.
- [15] A. R. Rezaei *et al.*, "Noninvasive hippocampal blood-brain barrier opening in alzheimers disease with focused ultrasound," *Proceedings of the National Academy of Sciences*, vol. 117, no. 17, pp. 9180–9182, 2020.
- [16] A. Abrahao *et al.*, "First-in-human trial of blood-brain barrier opening in amyotrophic lateral sclerosis using MR-guided focused ultrasound," *Nature communications*, vol. 10, no. 1, pp. 1–9, 2019.
- [17] K. Hynynen and G. Clement, "Clinical applications of focused ultrasound - the brain," *International Journal of Hyperthermia*, vol. 23, no. 2, pp. 193–202, 2007.
- [18] F. Fry and J. Barger, "Acoustical properties of the human skull," *The Journal of the Acoustical Society of America*, vol. 63, no. 5, pp. 1576–1590, 1978.
- [19] S. Pichardo *et al.*, "Multi-frequency characterization of the speed of sound and attenuation coefficient for longitudinal transmission of freshly excised human skulls," *Physics in Medicine & Biology*, vol. 56, no. 1, pp. 219–250, 2010.
- [20] J. G. Lynn *et al.*, "A new method for the generation and use of focused ultrasound in experimental biology," *The Journal of general physiology*, vol. 26, no. 2, pp. 179–193, 1942.
- [21] G. T. Clement *et al.*, "A hemisphere array for non-invasive ultrasound brain therapy and surgery," *Physics in Medicine & Biology*, vol. 45, no. 12, p. 3707, 2000.
- [22] G. T. Clement and K. Hynynen, "A non-invasive method for focusing ultrasound through the human skull," *Physics in Medicine & Biology*, vol. 47, no. 8, pp. 1219–1236, 2002.
- [23] J. White *et al.*, "Transcranial ultrasound focus reconstruction with phase and amplitude correction," *Ieee transactions on ultrasonics, ferroelectrics, and frequency control*, vol. 52, no. 9, pp. 1518–1522, 2005.
- [24] N. McDannold, "Quantitative MRI-based temperature mapping based on the proton resonant frequency shift:

Review of validation studies,” *International journal of hyperthermia*, vol. 21, no. 6, pp. 533–546, 2005.

[25] N. D. Doolittle *et al.*, “Safety and efficacy of a multicenter study using intraarterial chemotherapy in conjunction with osmotic opening of the blood-brain barrier for the treatment of patients with malignant brain tumors,” *Cancer*, vol. 88, no. 3, pp. 637–647, 2000.

[26] I. Tamai and A. Tsuji, “Transporter-mediated permeation of drugs across the blood–brain barrier,” *Journal of pharmaceutical sciences*, vol. 89, no. 11, pp. 1371–1388, 2000.

[27] Y. Taché *et al.*, “Inhibition of gastric acid secretion in rats by intracerebral injection of corticotropin-releasing factor,” *Science*, vol. 222, no. 4626, pp. 935–937, 1983.

[28] D. McMahon *et al.*, “Evaluating the safety profile of focused ultrasound and microbubble-mediated treatments to increase blood-brain barrier permeability,” *Expert opinion on drug delivery*, vol. 16, no. 2, pp. 129–142, 2019.

[29] L. Bakay *et al.*, “Ultrasonically produced changes in the blood-brain barrier,” *AMA Archives of Neurology & Psychiatry*, vol. 76, no. 5, pp. 457–467, 1956.

[30] K. Hynynen *et al.*, “Noninvasive MR imaging–guided focal opening of the blood-brain barrier in rabbits,” *Radiology*, vol. 220, no. 3, pp. 640–646, 2001.

[31] D. McMahon and K. Hynynen, “Acute inflammatory response following increased blood-brain barrier permeability induced by focused ultrasound is dependent on microbubble dose,” *Theranostics*, vol. 7, no. 16, p. 3989, 2017.

[32] N. Asquier *et al.*, “Blood-brain barrier disruption in humans using an implantable ultrasound device: Quantification with MR images and correlation with local acoustic pressure,” *Journal of neurosurgery*, vol. 1, no. aop, pp. 1–9, 2019.

[33] L. Goldwirt *et al.*, “Enhanced brain distribution of carboplatin in a primate model after blood–brain barrier disruption using an implantable ultrasound device,” *Cancer chemotherapy and pharmacology*, vol. 77, no. 1, pp. 211–216, 2016.

[34] A. Carpentier *et al.*, “Clinical trial of blood-brain barrier disruption by pulsed ultrasound,” *Science translational medicine*, vol. 8, no. 343, 343re2–343re2, 2016.

[35] K. Wei *et al.*, “Neuronavigation-guided focused ultrasound-induced blood-brain barrier opening: A preliminary study in swine,” *American Journal of Neuroradiology*, vol. 34, no. 1, pp. 115–120, 2013.

[36] A. N. Pouliopoulos *et al.*, “A clinical system for non-invasive blood–brain barrier opening using a neuronavigation-guided single-element focused ultrasound transducer,” *Ultrasound in medicine & biology*, vol. 46, no. 1, pp. 73–89, 2020.

[37] G. Maimbourg *et al.*, “3D-printed adaptive acoustic lens as a disruptive technology for transcranial ultrasound therapy using single-element transducers,” *Physics in Medicine and Biology*, vol. 63, no. 2, 2017.

[38] J. Aubry *et al.*, “Experimental demonstration of noninvasive transskull adaptive focusing based on prior computed tomography scans,” *The Journal of the Acoustical Society of America*, vol. 113, no. 1, pp. 84–93, 2003.

[39] R. M. Jones *et al.*, “Echo-focusing in transcranial focused ultrasound thalamotomy for essential tremor: A feasibility study,” *Movement Disorders*, pp. 2327–2333, 2017.

[40] C. Adams *et al.*, “Excitation and acquisition of cranial guided waves using a concave array transducer,” in *Proceedings of Meetings on Acoustics 173EAA*, ASA, vol. 30, 2017, p. 055 003.

[41] A. Kyriakou *et al.*, “A review of numerical and experimental compensation techniques for skull-induced phase aberrations in transcranial focused ultrasound,” *International journal of hyperthermia*, vol. 30, no. 1, pp. 36–46, 2014.

[42] L. Deng *et al.*, “A noninvasive ultrasound resonance method for detecting skull induced aberrations may provide a signal for adaptive focusing,” *IEEE Transactions on Biomedical Engineering*, pp. 2628–2637, 2020.

[43] K. J. Haworth *et al.*, “Towards aberration correction of transcranial ultrasound using acoustic droplet vaporization,” *Ultrasound in medicine & biology*, vol. 34, no. 3, pp. 435–445, 2008.

[44] G. W. Miller *et al.*, “Ultrashort echo-time MRI versus ct for skull aberration correction in MR-guided transcranial focused ultrasound: In vitro comparison on human calvaria,” *Medical physics*, vol. 42, no. 5, pp. 2223–2233, 2015.

[45] U. Vyas *et al.*, “Transcranial phase aberration correction using beam simulations and MR-ARFI,” *Medical physics*, vol. 41, no. 3, p. 032 901, 2014.

[46] N. Lipsman *et al.*, “Intracranial applications of magnetic resonance-guided focused ultrasound,” *Neurotherapeutics*, vol. 11, no. 3, pp. 593–605, 2014.

[47] A. Haritonova *et al.*, “In vivo application and localization of transcranial focused ultrasound using dual-mode ultrasound arrays,” *IEEE transactions on ultrasonics, ferroelectrics, and frequency control*, vol. 62, no. 12, pp. 2031–2042, 2015.

[48] FUS Foundation. (2021). Treatment sites, [Online]. Available: <https://www.fusfoundation.org/the-technology/treatment-sites?indication=Essential%20Tremor> (visited on 02/18/2021).

[49] A. Hughes and K. Hynynen, “Design of patient-specific focused ultrasound arrays for non-invasive brain therapy with increased trans-skull transmission and steering range,” *Physics in Medicine & Biology*, vol. 62, no. 17, pp. L9–L19, 2017.

[50] N. P. Ellens *et al.*, “A novel, flat, electronically-steered phased array transducer for tissue ablation: Preliminary results,” *Physics in Medicine & Biology*, vol. 60, no. 6, pp. 2195–2215, 2015.

[51] P. Aslani *et al.*, “Thermal therapy with a fully electronically steerable hifu phased array using ultrasound guidance and local harmonic motion monitoring,” *IEEE Transactions on Biomedical Engineering*, pp. 1854–1862, 2019.

- [52] A. Pulkkinen *et al.*, “Numerical simulations of clinical focused ultrasound functional neurosurgery,” *Physics in Medicine and Biology*, vol. 59, no. 7, pp. 1679–1700, 2014.
- [53] C. W. Connor *et al.*, “A unified model for the speed of sound in cranial bone based on genetic algorithm optimization,” *Physics in Medicine & Biology*, vol. 47, no. 22, pp. 3925–3944, 2002.
- [54] S. Pichardo and K. Hynynen, “Treatment of near-skull brain tissue with a focused device using shear-mode conversion: A numerical study,” *Physics in Medicine & Biology*, vol. 52, no. 24, pp. 7313–7332, 2007.
- [55] G. Clement *et al.*, “Enhanced ultrasound transmission through the human skull using shear mode conversion,” *The Journal of the Acoustical Society of America*, vol. 115, no. 3, pp. 1356–1364, 2004.
- [56] P. White *et al.*, “Longitudinal and shear mode ultrasound propagation in human skull bone,” *Ultrasound in medicine & biology*, vol. 32, no. 7, pp. 1085–1096, 2006.
- [57] J. Sun and K. Hynynen, “Focusing of therapeutic ultrasound through a human skull: A numerical study,” *The Journal of the Acoustical Society of America*, vol. 104, no. 3, pp. 1705–1715, 1998.
- [58] E. B. Saff and A. B. Kuijlaars, “Distributing many points on a sphere,” *The mathematical intelligencer*, vol. 19, no. 1, pp. 5–11, 1997.
- [59] K. Hynynen and R. M. Jones, “Image-guided ultrasound phased arrays are a disruptive technology for non-invasive therapy,” *Physics in Medicine & Biology*, vol. 61, no. 17, R206, 2016.
- [60] J. Song *et al.*, “Investigation of standing-wave formation in a human skull for a clinical prototype of a large-aperture, transcranial MR-guided focused ultrasound (MRgFUS) phased array: An experimental and simulation study,” *IEEE transactions on biomedical engineering*, vol. 59, no. 2, pp. 435–444, 2011.
- [61] S. Sokka *et al.*, “Spatial control of cavitation: Theoretical and experimental validation of a dual-frequency excitation method,” in *IEEE Ultrasonics Symposium, 2004*, IEEE, vol. 2, 2004, pp. 878–881.
- [62] R. M. Jones and K. Hynynen, “Advances in acoustic monitoring and control of focused ultrasound-mediated increases in blood-brain barrier permeability,” *The British journal of radiology*, vol. 92, no. 1096, p. 20180601, 2019.
- [63] L. Deng *et al.*, “A multi-frequency sparse hemispherical ultrasound phased array for microbubble-mediated transcranial therapy and simultaneous cavitation mapping,” *Physics in Medicine & Biology*, vol. 61, no. 24, pp. 8476–8501, 2016.
- [64] R. M. Jones *et al.*, “Three-dimensional transcranial microbubble imaging for guiding volumetric ultrasound-mediated blood-brain barrier opening,” *Theranostics*, vol. 8, no. 11, pp. 2909–2926, 2018.
- [65] R. M. Jones *et al.*, “Ultrafast three-dimensional microbubble imaging in vivo predicts tissue damage volume distributions during nonthermal brain ablation,” *Theranostics*, vol. 10, no. 16, pp. 7211–7230, 2020.
- [66] N. McDannold *et al.*, “Targeted disruption of the blood-brain barrier with focused ultrasound: Association with cavitation activity,” *Physics in Medicine & Biology*, vol. 51, no. 4, p. 793, 2006.
- [67] Y.-S. Tung *et al.*, “In vivo transcranial cavitation threshold detection during ultrasound-induced blood-brain barrier opening in mice,” *Physics in Medicine & Biology*, vol. 55, no. 20, p. 6141, 2010.
- [68] E. A. Neppiras, “Acoustic cavitation,” *Physics reports*, vol. 61, no. 3, pp. 159–251, 1980.
- [69] R. M. Jones *et al.*, “Experimental demonstration of passive acoustic imaging in the human skull cavity using ct-based aberration corrections,” *Medical physics*, vol. 42, no. 7, pp. 4385–4400, 2015.
- [70] M. A. O’Reilly and K. Hynynen, “Blood-brain barrier: Real-time feedback-controlled focused ultrasound disruption by using an acoustic emissions-based controller,” *Radiology*, vol. 263, no. 1, pp. 96–106, 2012.
- [71] M. A. O’Reilly *et al.*, “Registration of human skull computed tomography data to an ultrasound treatment space using a sparse high frequency ultrasound hemispherical array,” *Medical physics*, vol. 43, no. 9, pp. 5063–5071, 2016.